Multiferroic order and large magnetic refrigeration capacity in Gd_2MnFeO_6: Significance of magnetic frustration and Jahn-Teller distortion

A. Hati,[1] S. Mukherjee,[1] N. Mondal,[1] S. Bhowmik,[2] G. Manna,[3] S. Majumdar,[1] and S. Giri[1,*]

[1]*School of Physical Sciences, Indian Association for the Cultivation of Science, Jadavpur, Kolkata 700032, India*

[2]*Condensed Matter Physics Division, Saha Institute of Nuclear Physics, 1/AF, Bidhannagar, Kolkata 700064, India*

[3]*Chemistry and Physics of Materials Unit, Jawaharlal Nehru Centre for Advanced Scientific Research, Rachenahalli Lake Road, Jakkur, Bengaluru, Karnataka 560064, India*

(Received 8 May 2023; revised 30 August 2023; accepted 12 October 2023; published 25 October 2023)

We present a noteworthy finding of high-temperature ferroelectric order in a fairly unexplored Gd_2MnFeO_6 compound, characterized by a disordered double-perovskite structure. This material exhibits a remarkable cryogenic refrigerant capacity alongside the ferroelectric order, making it a rare occurrence. Notably, the refrigerant capacity of this Gd-based double perovskite surpasses that of all previously reported counterparts. Around 92 K (T_{FE}), we observe the presence of ferroelectric order, which is significantly higher in temperature compared to the magnetic order at 4 K (T_N). The involvement of dominant short-range magnetic order below T_{FE} ($\gg T_N$) leads to a notable magnetoelectric consequence. Raman studies further support our findings, revealing a steplike octahedral distortion of $(Mn/Fe)O_6$ at T_{FE}. This distortion aligns with a structural transition to a polar $Pna2_1$ structure at T_{FE}, consequently inducing the ferroelectric order. The high-temperature ferroelectric order associated with the linear magnetoelectric coupling and promising magnetic refrigeration capacity are in tune with the strong magnetic frustration and significant Jahn-Teller effect in Gd_2MnFeO_6.

DOI: 10.1103/PhysRevB.108.144431

I. INTRODUCTION

The double-perovskite oxides with the $A_2B'B''O_6$ formula continue to grow interest due to diverse ranges of the interesting properties and possible various applications in recent decades [1–3]. The perovskite structure is a robust structure, which can accommodate various elements in the periodic table [4]. It has been observed that the two different cations B'/B'' with close ionic radii usually form a disordered double-perovskite structure having *Pbnm* space group. The large difference between the ionic size, electronegativity, and oxidation states between B'/B'' cations is crucial to form an ordered structure with the $P2_1/n$ space group. Recent investigations on double perovskites indicate that an ordered double-perovskite structure with the monoclinic $P2_1/n$ space group favors the ferroelectric order, proposing different origins of the multiferroic orders [5–18]. On the contrary, ferroelectricity has been rarely reported for the disordered compounds with very few exceptions such as $YCr_{1-x}M_xO_3$ (M = Fe or Mn) [19] and Pr_2FeCrO_6 [20] having a disordered *Pbnm* structure at room temperature. In the first observation the ferroelectric polarization was reported to occur at the magnetic order in $YCr_{1-x}M_xO_3$ [19]. The origin of ferroelectricity was suggested due to the disordered cations of nonequivalent spins at the B site of weakly ferromagnetic perovskites. In the second observation, the emergence of a small value of the electric polarization was suggested due to the local noncentrosymmetric structure of Pr_2FeCrO_6, proposing a type-I multiferroic order [20].

The disordered double perovskite, Gd_2MnFeO_6 (GMFO) having *Pbnm* structure at room temperature has been less focused so far. Recently, the preliminary magnetic and optical properties were reported in nanocrystalline GMFO [21]. Probable Griffiths phase, spin reorientation, and promising magnetocaloric effect have been reported in polycrystalline GMFO [22]. To the best of our knowledge, further significant reports are not available on GMFO.

In the paper we report ferroelectric (FE) order close to 92 K (T_{FE}) in GMFO, where the origin of the spontaneous ferroelectric order is different from the previous very few reports having high-temperature disordered *Pbnm* structure. Heat capacity and dc magnetization results further reveal a magnetic order around 4 K. A significant magnetoelectric (ME) coupling is observed below T_{FE}, indicating that dominant short-range magnetic order is associated with the observed ME coupling. The ME response is linear below T_{FE}, which decreases with decreasing temperature and remains unchanged below ~60 K. The emergence of FE order is found to be associated with the structural transition to a polar structure with the $Pna2_1$ space group from the high-temperature *Pbnm* structure, which is confirmed by the temperature dependent synchrotron diffraction studies. The Raman spectroscopy as a function of temperature proposes the sharp $(Mn/Fe)O_6$ octahedral distortions around T_{FE}. The promising magnetocaloric effect with a change in entropy (ΔS_M) of ~16.7 J/kg K at 4 K and a maximum change in adiabatic temperature (ΔT_{ad}) of ~9 K at 10 K for a change in field of 0–50 kOe are observed from both the magnetic field dependent magnetization and heat capacity results. Magnetic refrigeration capacity is found to be larger than the reported Gd-based double perovskites. The combined promising refrigeration capacity and

*sspsg2@iacs.res.in

unexplored high-temperature multiferroic order associated with the linear ME, driven by the short-range magnetic order and significant Jahn-Teller effect, highlight GMFO as a potential candidate.

II. EXPERIMENTAL DETAILS

Polycrystalline Gd_2MnFeO_6 is prepared using a standard solid state reaction technique [23]. The single-phase purity of the sample is confirmed by the x-ray diffraction studies at room temperature recorded in a Rigaku Smart Lab 9 kW XG diffractometer equipped with a five-axis goniometer and using Cu $K\alpha$ radiation. Crystalline structure is further investigated using synchrotron radiation with a wavelength of $\lambda = 1.1514$ Å at the Photon Factory, National Laboratory for High Energy Physics (KEK), Japan, in the temperature range of 15–300 K. X-ray photoemission spectroscopy (XPS) is recorded with a spectrometer from Omicron Nanotechnology. A powder sample pressed into a pellet is used for the dielectric measurements using an E4980A LCR meter (Agilent Technologies, USA) equipped with a PPMS-II system from Quantum Design. The pyroelectric current (I_p) is recorded at a constant temperature sweep rate using an electrometer (Keithley, model 6517B), which is coupled with the PPMS-II. The specific heat is measured using a commercial PPMS-II Dyna Cool system. Temperature dependent Raman spectroscopy measurements are carried out using a Horiba T6400 Raman spectrometer (excitation wavelength = 532 nm with spot size 1 μm). The I_p is integrated over time for obtaining the spontaneous electric polarization. The poling electric field is applied during the cooling processes and the measurements are carried out in the warming mode with a zero electric field. Before the measurement of I_p the electrical connections are short circuited and waited for a sufficiently long time. In all the measurements the electrical contacts are fabricated using an air drying silver paint. Magnetization is measured in a commercial magnetometer of Quantum Design (magnetic property measurement system, evercool) in zero-field cooled (ZFC) mode until 360 K. High-temperature magnetization measurement is recorded up to 800 K using a vibrating sample magnetometer (model EV9, M/S Microsense, LLC Corp., USA). In the case of ZFC conditions, the sample is cooled in zero field (H) and the measurements are carried out in the warming mode in the presence of a field.

III. EXPERIMENTAL RESULTS AND DISCUSSIONS

A. Characterization of Gd_2MnFeO_6

The x-ray diffraction pattern recorded at 300 K is depicted in Fig. 1(a). Rietveld refinement is done satisfactorily using the *Pbnm* space group, as shown by the continuous curve. Lattice constants are obtained as $a = 5.3354(7)$ Å, $b = 5.6945(0)$ Å, and $c = 7.5801(9)$ Å with the reliability parameters $R_w(\%) \sim 4.01$, $R_{\text{expt.}}(\%) \sim 3.02$, and $\chi^2 \sim 1.05$. The values of the lattice constants are consistent with the previous reports [23].

The Fe ($2p$), Mn ($2p$), and Gd ($4d$) core level XPS of GMFO are summarized in Figs. 1(b), 1(c), and 1(d), respectively. Figure 1(b) depicts the spectrum with the peaks at 724.7 and 710.7 eV for Fe $2p_{1/2}$ and $2p_{3/2}$, respectively. Figure 1(c) shows the spectrum with the peaks at 653.6 and 641.8 eV for $2p_{1/2}$ and $2p_{3/2}$ of Mn, respectively. Two peaks are observed at 141.8 and 147.4 eV in Fig. 1(d) corresponding to the $4d_{5/2}$ and $4d_{3/2}$ of Gd, respectively. The satisfactory fits are shown by the solid curves on the experimental data in all the figures. The results indicate the Gd^{3+}, Fe^{3+}, and Mn^{3+} states coexist in GMFO, as reported earlier [22,23]. We note that the ratio of the area under the curve of the Gd, Fe, and Mn spectrum is close to 2.03:1.01:0.997, which is reasonably close to the composition of Gd_2MnFeO_6.

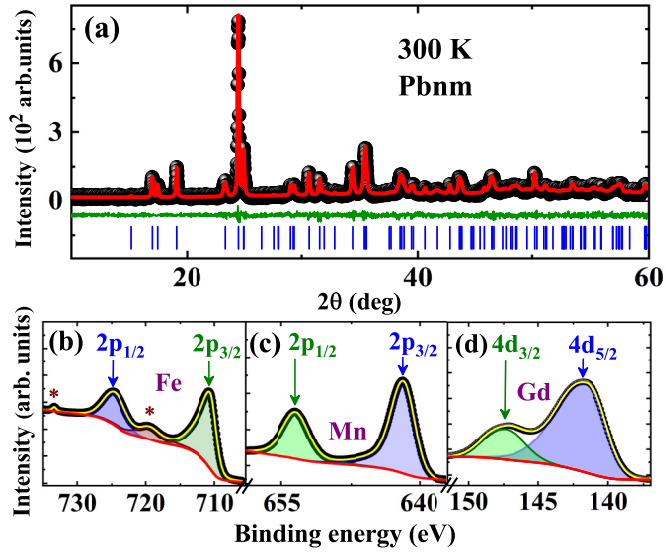

FIG. 1. (a) Rietveld refinement of the XRD pattern at 300 K. (b) Fe $2p$, (c) Mn $2p$, and (d) Gd $4d$ core level XPS of GMFO. Peaks indicated by "∗" show the satellite peaks.

B. Magnetizaton and magnetocaloric effect

Thermal variations of ZFC magnetization (M) recorded in different H are shown in Fig. 2(a). The value of M increases with the decrease in temperature (T). The M-T curves exhibit an indication of the onset of a peak at low T, which is further highlighted in the dM/dT curves, as depicted in Fig. 2(b). The dM/dT curves for different H exhibit a minimum at low T, which do not shift convincingly for different H. The thermal variation of the dM/dT curve recorded with 30 kOe exhibits a hump below the minimum, as indicated by a vertical broken line at 4 K, which is not so prominent for the low-field measurements. We further note that the heat capacity (C_P) results as a function of T show a well-defined maximum around 4 K [see lower inset of Fig. 3(a)], pointing to the occurrence of a magnetic order. Inverse dc susceptibility (χ^{-1}) as a function of T, recorded up to 360 K, is depicted in Fig. 2(c). At high temperature χ^{-1} follows the Curie-Weiss (CW) law, $\chi = C/(T - \theta_{CW})$ above ∼200 K, where C is the Curie constant and θ_{CW} is the Curie-Weiss temperature. The top inset of the figure further shows the $\chi(T)^{-1}(T)$ in log-log scale to highlight more clearly the deviation from the CW law around ∼200 K, as indicated by an arrow. To further check the Curie-Weiss fit, measurement was carried out until 800 K. Linear fit is shown in the bottom inset of the figure, which is consistent with the linear fit until

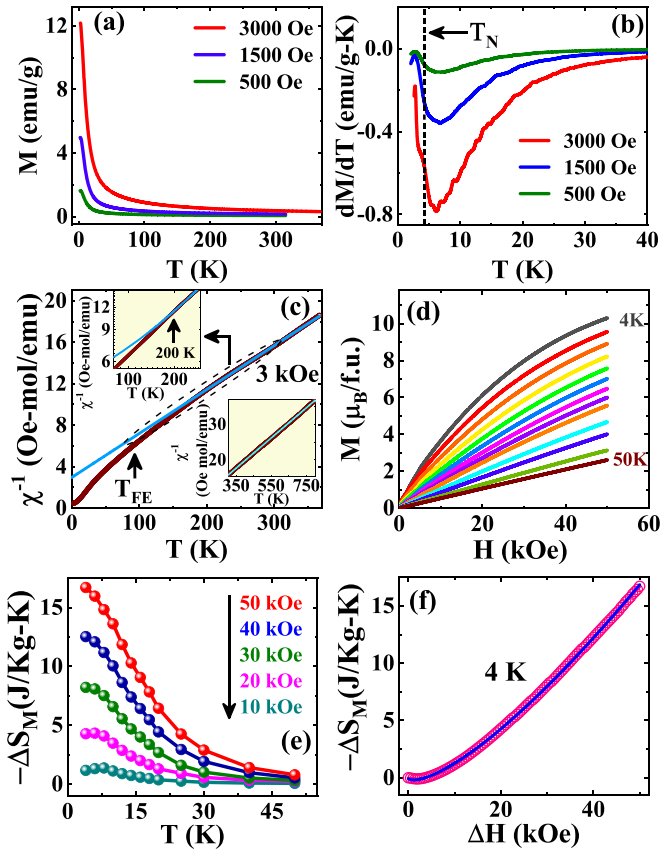

FIG. 2. The T variations of (a) ZFC magnetization (M) curves, (b) dM/dT curves recorded at different H, and (c) inverse susceptibility (χ^{-1}) recorded with $H = 3$ kOe. (d) Magnetization curves at selected T. (e) Magnetic entropy change (ΔS_M) with T for selected change in H (ΔH). (f) Plot of ΔS_M with ΔH at 4 K. Top inset of (c) further highlights deviation from the Curie-Weiss fit in a log-log scale around ∼200 K, as indicated by an arrow and the bottom inset exhibits Curie-Weiss fit in the high-T region.

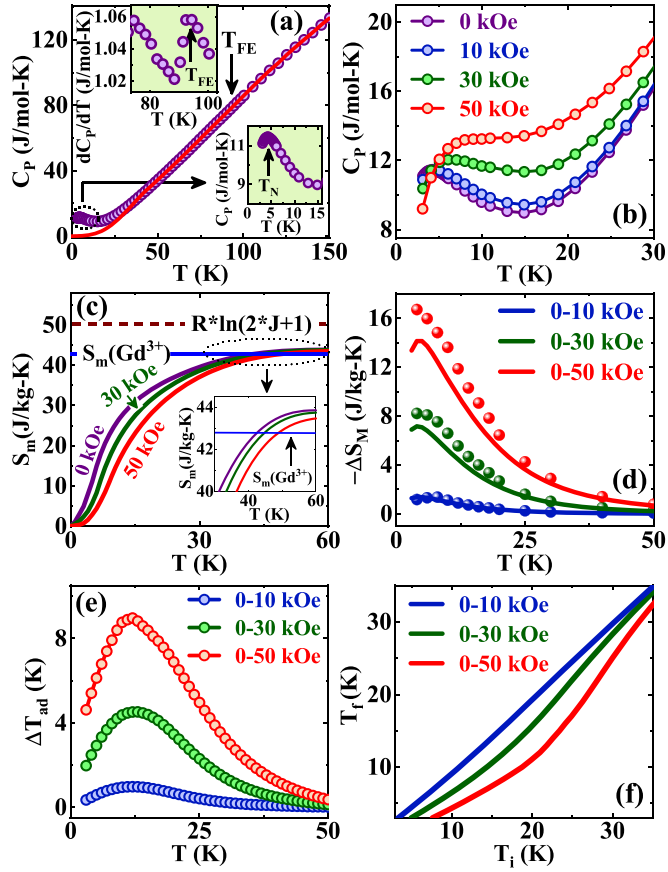

FIG. 3. The T variations of (a) heat capacity (C_P), (b) C_P at different field (H) at low temperature, (c) magnetic entropy (S_m), (d) ΔS_M, as obtained from the C_P (continuous curves) and compared with the same obtained from magnetization isotherm (symbol), (e) adiabatic temperature change (ΔT_{ad}), and (f) Plot of final temperature (T_f) against initial temperature (T_i) for different ΔH. Upper and lower insets of (a) highlight dC_P/dT close to FE order T_{FE} and C_P close to T_N, respectively. The inset of (c) further highlights the experimental results exceeding S_m for Gd^{3+}.

300 K. From a linear fit of $\chi^{-1}(T)$ in the high-temperature region the value of the effective paramagnetic moment is obtained as $\mu_{eff} = 13.75\,\mu_B$/f.u. with $\theta_{CW} = -69.0$ K. A large negative θ_{CW} suggests dominant antiferromagnetic exchange interaction in GMFO associated with a strong magnetic frustration parameter, $f \approx 17.25$. The value of μ_{eff} is found closer to the theoretical value (μ_{th}) of $13.6\,\mu_B$/f.u. considering $\mu_{th} = \sqrt{2\,\mu^2_{Gd^{3+}} + \mu^2_{Mn^{3+}} + \mu^2_{Fe^{3+}}}$ with $\mu_{Gd^{3+}} = 7.94\,\mu_B$, $\mu_{Mn^{3+}} = 4.9\,\mu_B$, and $\mu_{Fe^{3+}} = 5.92\,\mu_B$ [24].

Figure 2(d) depicts the magnetization curves at selected temperatures. The curves are nonlinear until ∼50 K, above which they show nearly linear dependence. The emergence of nonlinear magnetization curves is significant and suggests the presence of spin canting, which leads to an intricate ferromagnetic component well above T_N. Further investigations using microscopic experiments are necessary to gain insight into the ferromagnetic component even at temperatures considerably higher than T_N. The values of ΔS_M are derived from the magnetization isotherms using the Maxwell equation,

$$\Delta S_M(H,T) = \int_0^H [dM(H,T)/dT]_H dH.$$

Since the magnetization measurements are done at discrete field and at different temperature intervals, ΔS_M is calculated using the following expression:

$$\Delta S_M = \sum_i \frac{M_{i+1} - M_i}{T_{i+1} - T_i} \Delta H_i,$$

where M_i and M_{i+1} are the magnetic moments at temperatures T_i and T_{i+1}, respectively, for a small change in magnetic field H_i. The $\Delta S_M(T)$ has been deduced from the magnetic field dependence of the magnetization at different T using the above relation. The plots of ΔS_M with T for selected change of field (ΔH) are shown in Fig. 2(e). A large $\Delta S_M(T)$ is observed at lower temperature, which is considerable as 16.7 J/kg K for the field change of 0–50 kOe and agrees well with the recent report [22]. The H dependence of $-\Delta S_M$ is depicted in Fig. 2(f) at 4 K, which is close to T_N. The study on the field dependence of ΔS_M has been investigated either experimentally [25–27], or theoretically using a mean-field approach [28]. According to mean-field approximation, ΔS_M can be expressed as $\Delta S_M \propto H^n$ with an exponent, $n = 2/3$

at the magnetic order. The above relation does not hold in the current observation. The discrepancy has been explained recently [29] on the basis of Landau's theory of second-order phase transitions [30], which was applied to the spatially inhomogeneous ferromagnets. To fit the experimental results, we use $|\Delta S_M| = A(\Delta H + H_0)^{2/3} - AH_0^{2/3} + B(\Delta H)^{4/3}$, where A and B are the intrinsic parameters, whereas the inhomogeneity, if any, is taken care of by H_0 [31]. The parameters A, B, and H_0, as obtained from the fit, are -0.36 ± 0.06 J Kg^{-1} K^{-1} (kOe)$^{-2/3}$, 0.46 ± 0.06 J Kg^{-1} K^{-1} (kOe)$^{-4/3}$, and 1.25 ± 0.19 kOe, respectively, with a χ^2 value of 0.0065. The disorder occupancy of Fe^{3+} and Mn^{3+} at the octahedral site, driven by the disordered double-perovskite structure, may correlate with the nonzero H_0 term in the fitting. However, the values of the fitted parameters are consistent with the reported results [31].

C. Heat capacity in magnetic field

The MCE is further investigated by the heat capacity (C_P) measurements in the presence of field. The $C_P(T)$ recorded in zero field is shown in Fig. 3(a). The low-T $C_P(T)$ data is further highlighted in the lower inset of the figure, which shows a maximum around 4 K, suggesting a magnetic order. The result is consistent with the magnetization results, proposing T_N around 4 K. A weak change of slope in $C_P(T)$ is noted around FE order, which is further highlighted in the upper inset of the figure in the dC_P/dT-T plot. The $C_P(T)$ data fit with neither the Debye model nor the Einstein model solely. However, the combined Debye and Einstein models satisfactorily fits the experimental data using [32–36], $C_p(T) = pD(\theta_D, T) + (1 - p)E(\theta_E, T) + \gamma T$. The combined Debye and Einstein models represent the acoustic and optical phonon-mode contributions, respectively, to the heat capacity [37]. The best fit is shown by the solid curve in Fig. 3(a) with the Debye temperature, $\theta_D = 278$ K, Einstein temperature, $\theta_E = 610$ K, $\gamma = 0.03$ J/mol K^2, and $p = 0.28$. We note that the fitted solid curve deviates from the experimental $C_P(T)$ curve at low temperature. The low-T $C_P(T)$ is further highlighted in Fig. 3(b) recorded in different magnetic fields. Here, the lattice heat capacity data, as calculated from the combined Debye and Einstein models, is subtracted from the experimental $C_P(T)$ data to calculate the magnetic contribution (C_m). The magnetic entropy (S_m) is thus obtained by integrating $(C_m/T)dT$. Since we do not have $C_P(T)$ data below 2.5 K, the entropy change is determined by interpolating the $C_P(T)$ curves between 0 and 2.5 K using the standard methods [38]. The fully saturated value of $R \ln(2J + 1)$ with $R = 8.31$ J/mol K is shown by the broken straight line in Fig. 3(c) by taking into account the contribution from Gd^{3+}, Mn^{3+}, and Fe^{3+} spins. The solid line exhibits the saturated value considering the Gd^{3+} spin only. Figure 3(c) indicates that S_m starts to saturate above ~50 K. The saturated experimental value is found to be considerably lower than the fully saturated theoretical value. However, it is slightly higher than the theoretical value of S_m when considering only Gd^{3+} spin. The results indicate that either minor contributions from the Mn^{3+} and Fe^{3+} moments or the orbital contribution from the Gd moment contributes to S_m, in addition to the major contribution from Gd^{3+}.

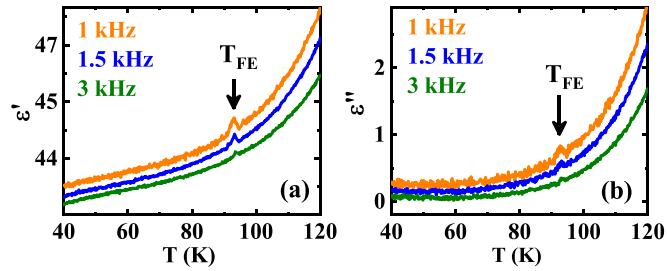

FIG. 4. Thermal variations of (a) real (ϵ') and (b) imaginary (ϵ'') components of dielectric constant.

To compare the magnetic entropy change as estimated from the magnetization isotherms, the $\Delta S_M(T)$ is calculated independently from the $C_P(T)$ data in the field using $\Delta S_M = \int_0^T [C_P(H_2, T) - C_P(H_1, T)]/T\, dT$, where $C_P(H, T)$ is the heat capacity as a function of H and T. The continuous curves in Fig. 3(d) show the ΔS_M with T for different H and is compared with the values of ΔS_M (symbol), as obtained from the magnetization isotherms. The values of $\Delta S_M(T)$, as obtained from heat capacity, are smaller than the values obtained from the magnetization results. The small difference might be attributed to the underestimation of the magnetic heat capacity.

Magnetic refrigeration has been further tested by calculating adiabatic temperature change (ΔT_{ad}). The isentropic temperature change between the entropy curves $S(H, T)$ and $S(0, T)$ provides the value of ΔT_{ad} [39]. Figure 3(e) shows the temperature dependence of ΔT_{ad} for different ΔH. The maximum value of ΔT_{ad} is observed to be ~9 K at ~10 K, which is considerable for a moderate change in ΔH of 50 kOe. We note an asymmetry in the $\Delta T_{ad}(T)$ curve at about 10 K, when applying a field adiabatically (ΔT_{ad} heating) and removing the field adiabatically (ΔT_{ad} cooling). The cooling effect can be realized due to the adiabatic removal of magnetic field, as depicted in Fig. 3(f) for different changes in ΔH. The final temperature (T_f) can be obtained by an adiabatic demagnetization from an initial temperature (T_i). The plots of T_f vs T_i for different changes in ΔH are depicted in Fig. 3(f). For example, the figure demonstrates that the T_i around 10 K has been reduced to ~3.5 K for a change in ΔH of 50 kOe, which is considerable and comparable to the results of the promising compounds [40,41].

D. Dielectric permittivity, ferroelectric order, and magnetoelectric coupling

The dielectric permittivity is recorded with T for different frequencies (f) in zero magnetic field. Thermal variations of the real (ϵ') and imaginary (ϵ'') components of dielectric permittivity are depicted in Figs. 4(a) and 4(b), respectively, for selected f at 1, 1.5, and 3 kHz. The figures show a weak anomaly around 92 K in both $\epsilon'(T)$ and $\epsilon''(T)$. The temperature at which anomaly is observed does not change convincingly with f, though the signature of anomaly weakens with an increase in f. The observation of anomaly at the same temperature in $\epsilon'(T)$ and ϵ'' primarily indicates the onset of the spontaneous polar order at T_{FE}. The result is quite similar to that reported weak anomaly in $Co_2Mo_3O_8$ [42],

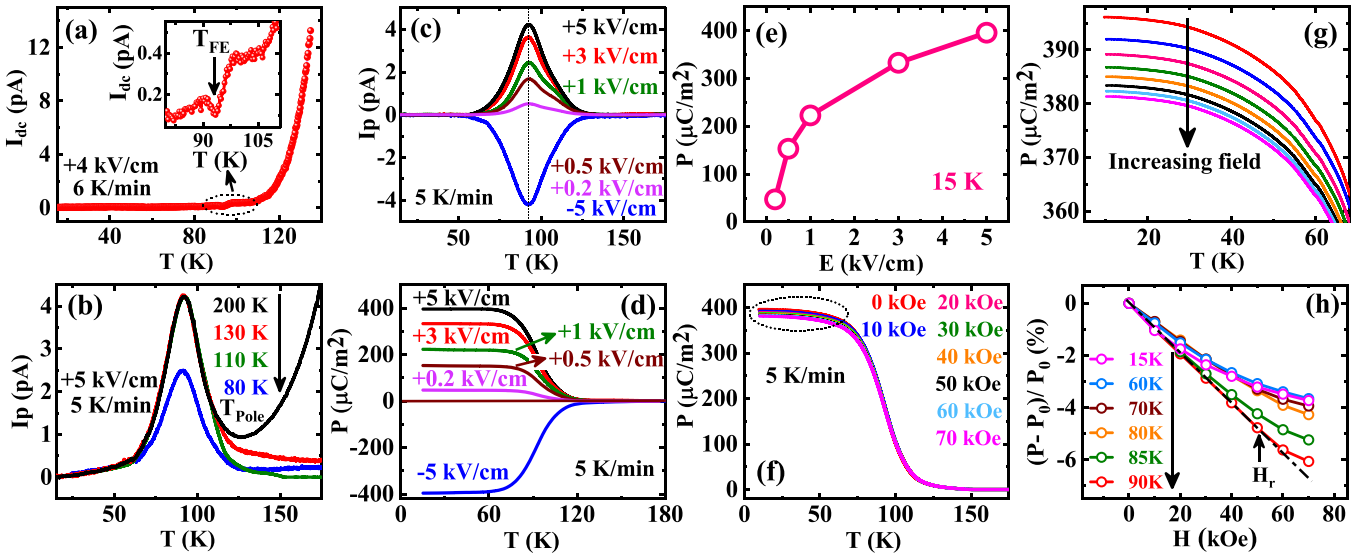

FIG. 5. The T variations of (a) I_{dc} recorded in a constant T-sweep rate of 6 K/min. The inset magnifies the region, where a minimum is observed. The T variations of (b) I_p for different poling temperatures (T_{pole}), as described in the text and for a poling field (E) of 5 kV/cm; and (c) I_p for $E = \pm 5, +3, +2, +1, +0.5$, and $+0.2$ kV/cm. (d) P at corresponding E values. (e) P vs E at 15 K. The T variation of (f) P at different magnetic fields (H) for $E = 5$ kV/cm. (g) Magnified variation of $P(T)$ with H. (h) Percentage of $(P - P_0)/P_0$ with H at selected temperatures. Downward arrow demonstrates curves with increasing temperature. The linear dependence of $(P - P_0)/P_0$ with H at 90 K is indicated by the broken straight line. H_r is the critical field, above which $(P - P_0)/P_0$ with H deviates from linearity.

$Na_2Co_2TeO_6$ [43], and (Y,R)CrO_4 (R = Sm, Gd, Ho) [44], and in contrast to the convincing absence of signature at the ferroelectric ordering temperature in $SmCrO_3$ [45], $HoFeO_3$ [46], and $NiFe_2O_4$ [47].

To confirm occurrence of a polar order, the dc bias current (I_{dc}) is recorded using a bias electric (BE) field method [48,49]. For the BE method the sample is cooled in zero electric field and I_{dc} is recorded in the warming mode in the presence of a bias electric field. Thermal variation of I_{dc} with a BE field of 4 kV/cm and a temperature scan rate of 6 K/min is shown in Fig. 5(a). The inset of the figure magnifies a selected temperature region, where a definite signature of a "dip" is observed around ∼92 K and confirms a polar order. The pyroelectric current (I_p) is recorded for different poling temperatures (T_{pole}) with a +5 kV/cm poling field (E). For I_p measurements the sample is always cooled from the selected T_{pole} down to a lowest measured temperature and I_p is measured during the warming mode in a zero poling field. The results of I_p with T at different T_{pole} are depicted in Fig. 5(b) for a heating rate of 5 K/min. In all of the cases, a peak is always observed around ∼92 K, at which a dip is observed in $I_{dc}(T)$ and further confirms the polar order (T_{FE}).

After subtracting the high-temperature thermally stimulated depolarization current (TSDC) component [50], the values of $I_p(T)$ are shown in Fig. 5(c) for different E. We note that the $I_p(T)$ reverses when negative E is applied, pointing to ferroelectric order. For obtaining thermal variations of the ferroelectric polarization (P), the $I_p(T)$'s are integrated over time, which are shown in Fig. 5(d) for different E values. To check the reproducibility of $P(T)$, the $I_p(T)$'s are recorded at different temperature sweep rates, while the integration over time for all the cases nearly reproduces the $P(T)$ over the recorded temperature region. With decreasing T the P value saturates below ∼60 K. The saturated value is ∼396 μC/m^2 for $E = 5$ kV/cm. Nevertheless, the contribution from the extrinsic TSDC component to the P value cannot be dismissed. This is due to the typical reduction of the extrinsic component as E values decrease [50]. Figure 5(e) shows a plot of P with E, for example, at 15 K. The P value increases with E and exhibits a saturating trend at $E = 5$ kV/cm. The P value is also influenced by the magnetic field. The values of $P(T)$ at different H are depicted in Fig. 5(f). Figure 5(g) magnifies the low-T results, which indicates a decrease in P with increasing H. The percentages of $(P - P_0)/P_0$ with H at selected temperatures are plotted in Fig. 5(h), where P_0 is the P value in zero field. At 90 K the P decreases almost linearly below ∼50 kOe. The value of the critical field (H_r), where the plot deviates from the linearity, decreases with decreasing T, as indicated in the figure. We note that the maximum change in polarization is observed below T_{FE} at 90 K, which is ∼6% for a 50-kOe magnetic field. The change in polarization due to magnetic field reduces with decreasing temperature and becomes nearly stable when the electric polarization saturates below ∼60 K.

The change in $P(T)$ at T_{FE} involves the entropy change (ΔS_E) attributed to the change in E (ΔE), which can be obtained from the Maxwell relation $(\frac{\delta S}{\delta E})_T = (\frac{\delta P}{\delta T})_E$ using

$$\Delta S_E = \frac{1}{\rho}\int_{E1}^{E2}\left(\frac{\delta P}{\delta T}\right)_E dE,$$

where ρ is the mass density [51]. $E1$ and $E2$ are the initial and final electric field, respectively. Thus, ΔS_E is calculated as a function T close to T_{FE}. The T variation of ΔS_E for selected ΔE is depicted in Fig. 6(a). The value of ΔS_E is

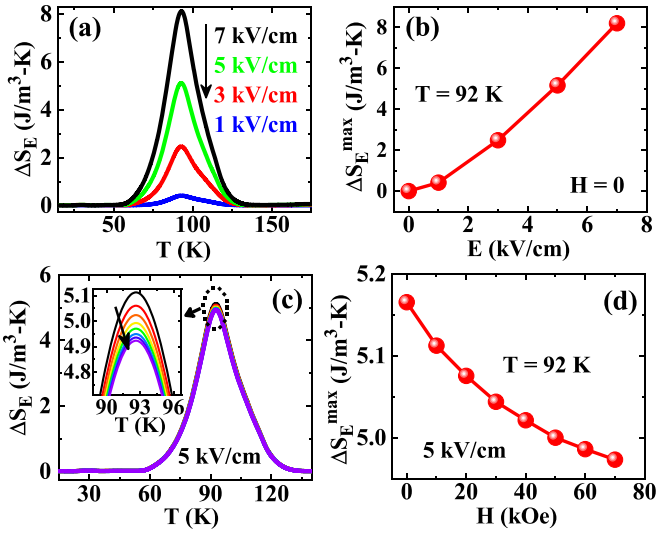

FIG. 6. Thermal variation of (a) ΔS_E at different E and (c) ΔS_E at different H. The inset of (c) highlights the peak region showing the decrease of ΔS_E with increasing H following $H = 0$, 10, 20, 30, 40, 50, 60, and 70 kOe, as indicated by an arrow. Plots of (b) $\Delta S_E^{\max}$ with ΔE and (d) $\Delta S_E^{\max}$ with H at 92 K, close to T_{FE}.

found maximum at T_{FE}. The maximum value of ΔS_E ($\Delta S_E^{\max}$) is significant as $\sim$8 J/m^3 K for $\Delta E = 7$ kV/cm, which is comparable to that observed for multicaloric $CoCr_2S_4$ [52], geometrically frustrated multiferroic $CaBaCo_4O_7$ [53], and multiferroic Y_2CoMnO_6 [54]. The plot of $\Delta S_E^{\max}$ with ΔE at T_{FE} is shown in Fig. 6(b). The influence of H on ΔS_E is recorded for a poling field of 5 kV/cm, which is depicted in Fig. 6(c). The change in ΔS_E close to T_{FE} is further highlighted in the inset of the figure. The decrease in $\Delta S_E^{\max}$ with H at 92 K is depicted in Fig. 6(d), pointing to a considerable multicaloric effect.

E. Raman spectra and octahedral distortion

To correlate FE order to the local structural distortion, the Raman spectra are recorded around T_{FE}. Figure 7(a) depicts a Raman spectrum at 300 K. We observe the strongest mode at around 650 cm^{-1} in the recorded spectral range, which is assigned due to the stretching vibration of the $(Mn/Fe)O_6$ octahedra [55,56]. The inset of the figure magnifies the peak for selected temperatures around T_{FE}. We note that the peak structure changes noticeably around T_{FE}. The Raman peaks recorded at 98 and 88 K are deconvoluted into two peaks such as "peak 1" and "peak 2," as shown in Figs. 7(b) and 7(c), respectively. Here, we use the Gaussian profile to fit the peak. The peak position, width, and integrated intensities of the Gaussian profiles, defined as peak 1 and peak 2, are followed with temperatures close to the ferroelectric order. The peak shift, full width at half maximum (FWHM), and integrated intensities for peak 1 and peak 2 are depicted in Figs. 7(d), 7(e), and 7(f), respectively. We observe a steplike decrease in the peak shift, FWHM, and integrated intensities at T_{FE}, as shown by a vertical broken straight line. The results indicate a

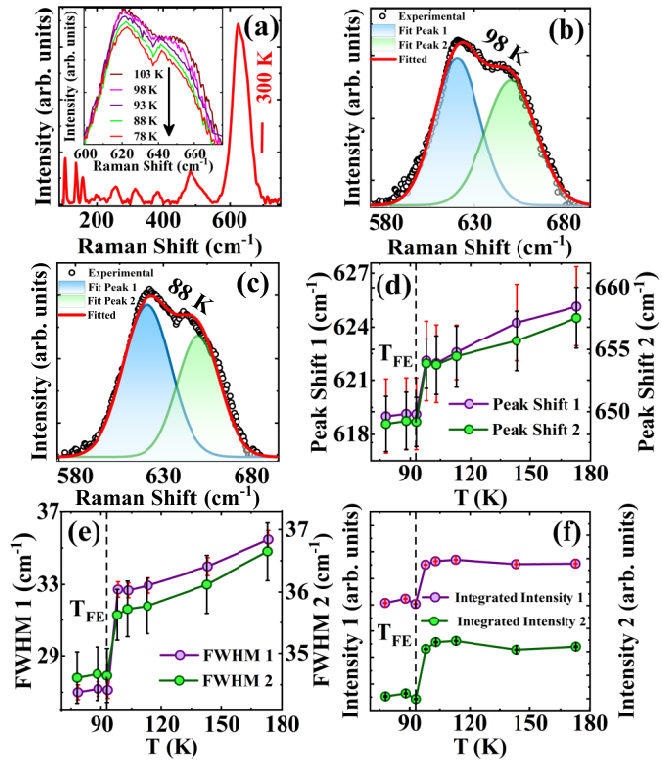

FIG. 7. (a) Raman spectrum at 300 K of GMFO. The inset shows an enlarged view of the 600–670 cm^{-1} spectral range at selected T around T_{FE}. Deconvolution of the spectrum at (b) 98 K and (c) 88 K in the range of 575–700 cm^{-1}. (d) Peak shifts, (e) full width at half maximum (FWHM), and (f) integrated intensities of both the deconvoluted peaks with T around T_{FE}.

significant $(Mn/Fe)O_6$ octahedral distortion at T_{FE}, proposing a possible structural transition at T_{FE}.

F. Structural transition at ferroelectric order

The structural properties are investigated by recording synchrotron diffraction patterns in the range of 15–300 K. The (004) diffraction peak, as highlighted in Fig. 8(c), is magnified in Fig. 8(a), which shows a decrease in peak height with decreasing temperature. The integrated intensity of a peak is plotted with temperature in Fig. 8(b), which demonstrates a sharp decrease below T_{FE}. The signature around T_{FE} is associated with the change in scattering cross section and indicates a possible structural transition. In fact, we try to refine the diffraction pattern below T_{FE} with the *Pbnm* space group, which is not satisfactory. We use the ISODISTORT [57] software to identify the possible structure below the proposed structural transition. We note that $Pna2_1$ (No. 33) fits satisfactorily, which has the highest symmetry among the recommended space groups. Thus the refinement of the synchrotron diffraction pattern at 92 K is done using the $Pna2_1$ space group, as shown in Fig. 8(c). For better clarification, the refinements of a peak around 35.6° using the *Pbnm* and $Pna2_1$ space groups are depicted by the solid curves in Figs. 8(d) and 8(e), respectively. We note a better fit of the peak using the $Pna2_1$ space group compared to the *Pbnm* structure, which is consistent

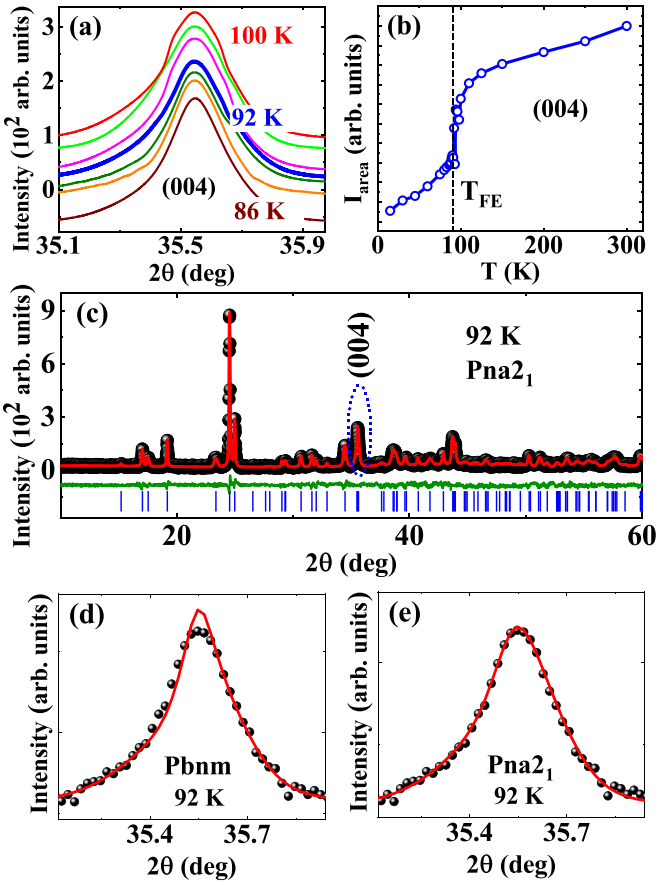

FIG. 8. (a) The peak observed close to 35.6° at selected temperatures around T_{FE} at 92 K. Thermal variation of (b) the integrated intensity of the peak observed close to 35.6°. (c) Rietveld refinement of the diffraction pattern at 92 K using the $Pna2_1$ space group. Refinements of a peak around 35.6° at 92 K (below structural transition) using the (d) $Pbnm$ and (e) $Pna2_1$ space groups, as indicated by the continuous curves.

with results for $RCrO_3$, revealing ferroelectric order at the similar structural transition [45,58,59]. The refinements of the diffraction patterns in the temperature range of 93–300 K are performed using $Pbnm$, and $Pna2_1$ is used for the refinements below 93 K. We note that reliability parameters are quite close for the entire temperature range, pointing to satisfactory refinements.

Thermal variations of the lattice constants a, b, and c, as obtained from the refinements, are depicted in Figs. 9(a), 9(b), and 9(c), respectively, whereas the unit cell volume (V) is depicted in Fig. 9(d). Figure 10(a) depicts connecting $(Mn/Fe)O_6$ octahedra within the unit cell. To observe octahedral distortion at T_{FE}, the average Mn/Fe-O1, Mn/Fe-O2, and Mn/Fe-O3 bond lengths are plotted with T in Fig. 10(b), which demonstrate a steplike change at the structural transition. We note that the increase of Mn/Fe-O2 is ∼4.3%, where the decreases of Mn/Fe-O1 and Mn/Fe-O3 are ∼1.5% and ∼2.3%, respectively. In the left panel of Fig. 10(c), the positions of the oxygen atoms (O1, O2, and O3) are shown in an octahedron. The right panel of the figure shows the octahedral distortion below T_{FE}, where contractions of the octahedra are shown along the directions of the apex O1 atom

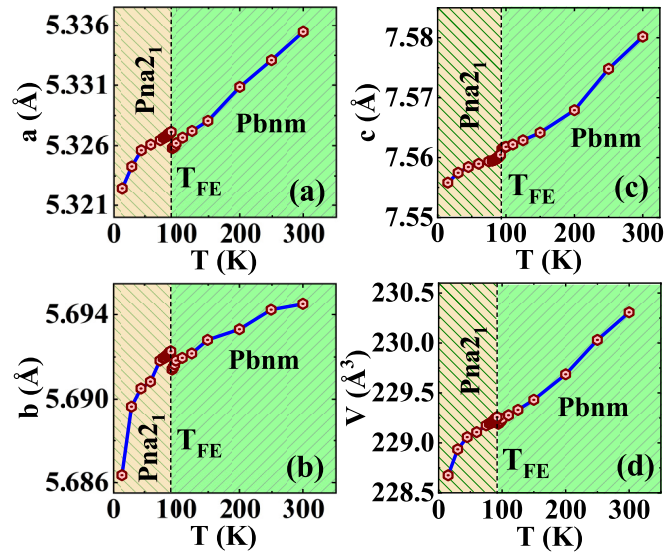

FIG. 9. Thermal variations of lattice constants: (a) a, (b) b, (c) c, and (d) unit cell volume (V).

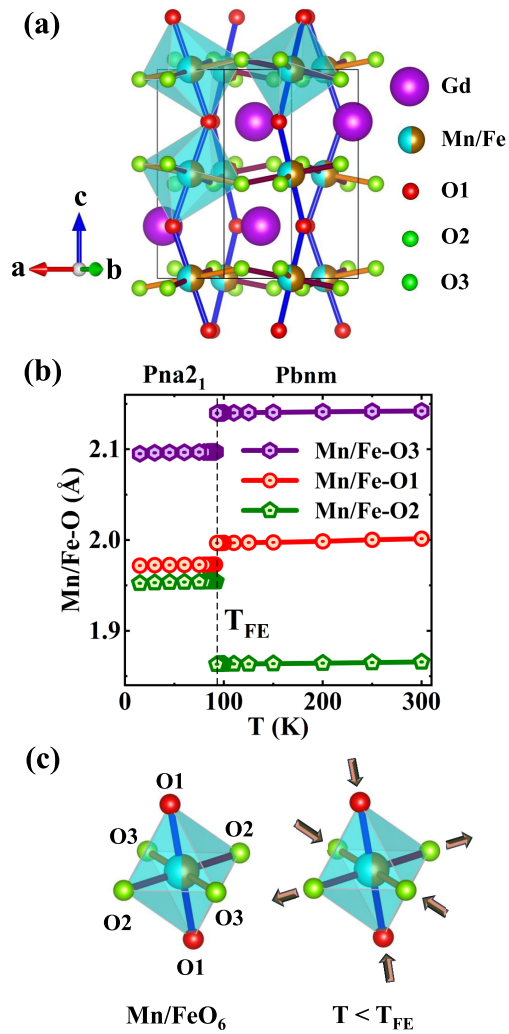

FIG. 10. (a) Connecting octahedra within the unit cell of Gd_2MnFeO_6. (b) T variations of Mn/Fe-O_6 bond lengths. (c) Distortion of Mn/FeO_6 octahedra below the structural transition.

TABLE I. Promising results of magnetocaloric effect in Gd-based double perovskites.

Samples	$-\Delta S_M$ (J/Kg−K)	T_N (K)	H (kOe)	ΔT_{ad} (K)	δT(K) FWHM	Ref.
Gd_2CoMnO_6	15	5	50	4	20	[63]
Gd_2NiMnO_6	23.2	10.5	50	9.5	20	[63]
$GdSrCoFeO_6$[a]	10.5	5	50	–	–	[64]
Gd_2ZnTiO_6	38	3	50	20	19	[65]
Gd_2ZnMnO_6	14	6.4	50	–	10[b]	[66]
Gd_2MgTiO_6	34	2.5	50	–	8[b]	[67]
Gd_2FeCoO_6	12	4.9	50	–	–	[68]
Gd_2FeAlO_6	18	<2	50	–	–	[69]
Gd_2MnFeO_6	16.7	4	50	9.0	23	Current

[a]Disordered double perovskite.
[b]Calculated from ΔS_M value.

and the basal O3 atom. The expansion is shown along the basal O2 direction, as depicted by the arrows.

G. Magnetic frustration and refrigeration capacity

The current investigation mainly focuses on the promising magnetocaloric effect and the rare occurrence of ferroelectricity in a disordered double-perovskite structure of Gd_2MnFeO_6. The magnetization results clearly indicate strong magnetic frustration with $f \approx 17.25$. In fact, the paramagnetic Curie-Weiss behavior deviates significantly above the proposed magnetic ordering temperature, suggesting a dominant short-range magnetic order. This observation is consistent with the disordered double-perovskite structure [3]. We note that at 300 K the average B-site metal-oxygen bond lengths are 2.0015(9), 1.8656(8), and 2.1423(0) Å for Mn/Fe-O1, Mn/Fe-O2, and Mn/Fe-O3, respectively. The nearest-neighbor (NN) and next-nearest neighbor (NNN) bond lengths of Gd-O1 are 2.1998(4) and 2.3460(3) Å, while for Gd-O2, they are 2.4385(1) and 2.4784(0) Å at 300 K. These values indicate that the NN and NNN interactions are comparable, leading to competing magnetic interactions that contribute to the observed magnetic frustration. Recent trends suggest that magnetic frustration plays a significant role in enhancing refrigeration capacity, as reported in studies [60–62]. The refrigeration capacity is defined as the maximum value of $|\Delta S_M| \times$ FWHM, as estimated from the ΔS_M vs T plot. In this case, the peak in ΔS_M is observed around 5 K, making it impossible to estimate FWHM. Instead, we rely on the ΔT vs T plot, which provides insight into the refrigeration capacity. The ΔT vs T plot reveals that the FWHM is ∼23 K, which is a significant value. The results of magnetic refrigeration of Gd-based double perovskite oxides are presented in Table I, which includes the current findings. It is worth noting that most promising results have been observed in the ordered double-perovskite structures, while reports on promising results for disordered double perovskites are relatively rare. However, in the current study, the observed FWHM is the highest among Gd-based double perovskites (Table I). Additionally, it exhibits reasonably high values of $|\Delta S_M|$ and ΔT_{ad}, which indicates a promising potential for high refrigeration capacity. We propose that the significant magnetic frustration

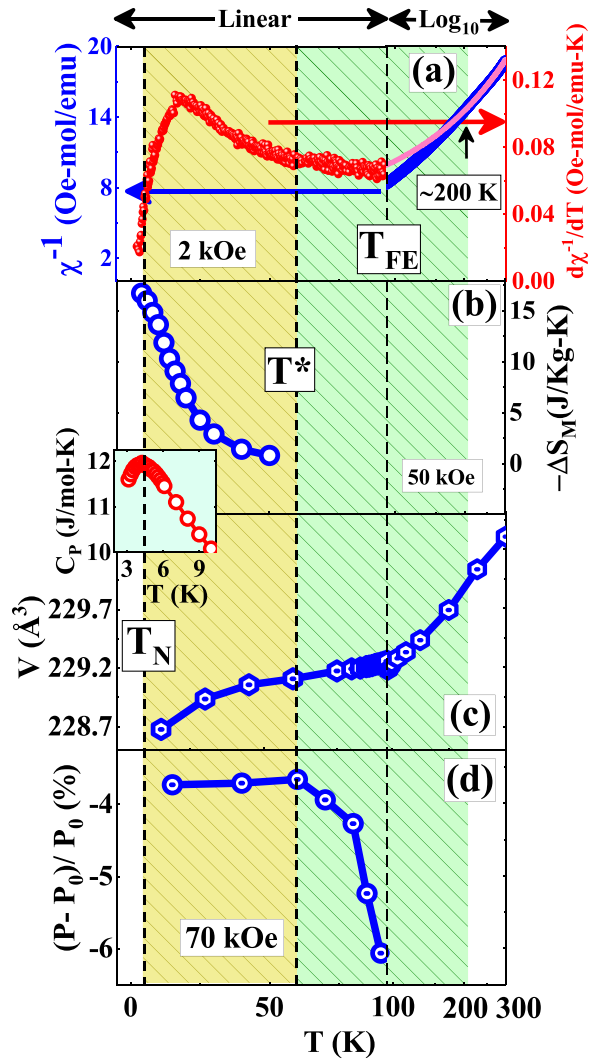

FIG. 11. Thermal variations of (a) χ^{-1} (left axis) and $d\chi^{-1}/dT$ (right axis), (b) $-\Delta S_M$, (c) V, and (d) $(P - P_0)/P_0$ (%). The inset shows $C_P(T)$, highlighting T_N. The different highlighted regions are discussed in the text.

associated with the disordered double-perovskite structure of GMFO contributes to the large ΔT, consistent with recent observations [3,60–62].

H. Ferroelectric order in a disordered double-perovskite structure

The emergence of a structural transition could be correlated with the presence of strong magnetic frustration, as this transition may potentially facilitate the release of magnetic frustration in the observed phenomenon. Another reason for the octahedral distortion associated with the structural transition around T_{FE} may be attributed to the presence of strong Jahn-Teller active Mn^{3+} ions in the compound. However, the probability of suppressing the cooperative Jahn-Teller distortion due to the 50% occupancy of Fe^{3+} cannot be disregarded. The suppression of Jahn-Teller distortion has been observed on a few occasions, such as in Fe- and Cr-substituted La_2MnCrO_3 [70] and La_2MnFeO_6 [70,71]. Nevertheless, evi-

dence of octahedral distortion driven by the Jahn-Teller effect was realized in La_2NiMnO_6 [72]. The lattice parameters can probe indirectly on the possible cooperative Jahn-Teller distortion. In the case of a Jahn-Teller distorted system three metal-oxygen bond lengths at the B site have been typically expected [73], which are realized in the current observation [Fig. 10(b)]. The signature of octahedral distortion has been realized from the Raman studies with decreasing temperature with a steplike sharp distortion near T_{FE}. At T_{FE}, a structural transition to a low-symmetry polar $Pna2_1$ structure has been realized, which eventually gives rise to the ferroelectric order. The symmetry analysis reveals that the distortion of $Pna2_1$ can be decomposed into two modes corresponding to the irreducible representations of nonpolar GM1+ and polar GM4−, where GM4− is the primary order parameter in this case. In a proper ferroelectric transition, all symmetries, including the inversion symmetry, are broken. However, in the current scenario, the $Pna2_1$ symmetry is an isotropy subgroup of $Pbnm$. Therefore, the transformation observed in the current study does not truly indicate a proper ferroelectric transition. Instead, it suggests an improper ferroelectric order in GMFO.

We would like to point out that the reported multiferroic orders in a few ordered perovskite materials have consistently been observed below the magnetic order [5–18], indicating typical type-II multiferroics. In contrast, the ferroelectricity in Gd_2MnFeO_6 occurs at much higher temperature than the magnetic order, which is similar to the behavior reported in another disordered perovskite, Pr_2FeCrO_6 [20]. Since multiferroic order has rarely been observed in disordered double perovskites, it is challenging to draw a definitive conclusion regarding the nature of the multiferroic order in GMFO. Elaborate investigations on the ferroelectric order in disordered double perovskites are required to gain further insights. As demonstrated in Fig. 11(a), the ferroelectric order occurs at a much lower temperature than the point where the magnetic susceptibility deviates from the linear Curie-Weiss behavior. These results suggest that the emergence of the ferroelectric order is associated with the dominant short-range magnetic order. Another important observation is the occurrence of ME effect just below T_{FE}, indicating a significant coupling between the dominant short-range magnetic order and the ME effect. The ME effect exhibits an intriguing behavior with temperature. Below T_{FE}, the change in P with H is linear, but the linearity decreases significantly with decreasing temperature. The thermal variation of ME response is depicted in Fig. 11(d), clearly showing that the response stabilizes around ∼60 K (T^*). T^* is a characteristic temperature below which magnetocaloric effect occurs, as shown in Fig. 11(b). The presence of T^* is also indicated by $d\chi^{-1}/dT$ and $V(T)$ curves in Figs. 11(a) and 11(c), respectively, where a minute change in slope is observed around T^*. Below T^*, the nonlinear magnetization curve starts to appear, pointing to different characteristic features of the short-range ordered state. Furthermore, we note that the magnetic entropy exhibits a saturating trend close to T^* based on the $C_P(T)$ results. The observation of an extended region of short-range order, divided into two regions above T_N, is believed to be correlated with strong magnetic frustration. However, the precise nature of the short-range order proposed here requires further exploration using microscopic experimental techniques.

IV. CONCLUSION

In conclusion, the current investigation suggests that the fairly unexplored disordered double perovskite Gd_2MnFeO_6 holds great promise as a potential candidate for both the intricate multiferroic order and large magnetic refrigeration capacity. Magnetic frustration enhances the large magnetic refrigeration capacity. The coexistence of strong magnetic frustration and significant Jahn-Teller distortion has been correlated with the emergence of intricate multiferroic order in Gd_2MnFeO_6. The remarkable magnetoelectric consequences observed, which vary with the temperature dependent nature of the short-range magnetic order, are intriguing. This finding has garnered attention from the scientific community, as it opens up possibilities for tuning magnetoelectric coupling by manipulating the short-range magnetic order.

ACKNOWLEDGMENTS

A.H. acknowledges UGC, India for support from a fellowship. S.G. acknowledges the SERB project No. CRG/2022/000718 for financial support and would also like to thank the Department of Science and Technology, India for financial support (Proposal No. ID-IB-2021-07) and Jawaharlal Nehru Centre for Advanced Scientific Research, India for facilitating the experiments at the Indian Beamline, Photon Factory, KEK, Japan. S.G. thanks the Technical Research Center of IACS, Kolkata, India for the heat capacity measurements. The authors acknowledge Chandan Mazumdar for the support of the high-temperature magnetization measurements.

[1] S. Vasala and M. Karppinen, Prog. Solid State Chem. **43**, 1 (2015).
[2] T. Saha-Dasgupta, Mater. Res. Express **7**, 014003 (2020).
[3] M. Alam and S. Chatterjee, J. Phys.: Condens. Matter **35**, 223001 (2023).
[4] A. S. Bhalla, R. Guo, and R. Roy, Mater Res. Innov. **4**, 3 (2000).
[5] N. Terada, D. D. Khalyavin, P. Manuel, W. Yi, H. S. Suzuki, N. Tsujii, Y. Imanaka, and A. A. Belik, Phys. Rev. B **91**, 104413 (2015).
[6] S. Chikara, J. Singleton, J. Bowlan, D. A. Yarotski, N. Lee, H. Y. Choi, Y. J. Choi, and V. S. Zapf, Phys. Rev. B **93**, 180405(R) (2016).
[7] H. Y. Zhou, H. J. Zhao, W. Q. Zhang, and X. M. Chen, Appl. Phys. Lett. **106**, 152901 (2015).
[8] J. T. Zhang, X. M. Lu, X. Q. Yang, J. L. Wang, and J. S. Zhu, Phys. Rev. B **93**, 075140 (2016).
[9] J. Blasco, J. García, G. Subías, J. Stankiewicz, J. A. Rodríguez-Velamazán, C. Ritter, J. L. García-Muñoz, and F. Fauth, Phys. Rev. B **93**, 214401 (2016).

[10] F. Yong, Y. Shi-Ming, Q. Wen, W. Wei, W. Dun-Hui, and D. You-Wei, Chin. Phys. B **23**, 117501 (2014).

[11] J. Su, Z. Z. Yang, X. M. Lu, J. T. Zhang, L. Gu, C. J. Lu, Q. C. Li, J.-M. Liu, and J. S. Zhu, ACS Appl. Mater. Interfaces **7**, 13260 (2015).

[12] S. Kumar, G. Giovannetti, J. van den Brink, and S. Picozzi, Phys. Rev. B **82**, 134429 (2010).

[13] H. Nhalil, H. S. Nair, C. M. N. Kumar, A. M. Strydom, and S. Elizabeth, Phys. Rev. B **92**, 214426 (2015).

[14] J. H. Kim, K. W. Jeong, D. G. Oh, H. J. Shin, J. M. Hong, J. S. Kim, J. Y. Moon, N. Lee, and Y. J. Choi, Sci. Rep. **11**, 23786 (2021).

[15] J. Krishnamurthya and A. Venimadhav, J. Magn. Magn. Mater. **500**, 166387 (2020).

[16] R. Takahashi, I. Ohkubo, K. Yamauchi, M. Kitamura, Y. Sakurai, M. Oshima, T. Oguchi, Y. Cho, and M. Lippmaa, Phys. Rev. B **91**, 134107 (2015).

[17] A. Rathi, H. Borkar, P. K. Rout, A. Gupta, H. K. Singh, A. Kumar, B. Gahtori, R. P. Pant, and G. A. Basheed, J. Phys. D: Appl. Phys. **50**, 465001 (2017).

[18] L. Wang, W. Zhou, D. Wang, Q. Cao, Q. Xu, and Y. Du, J. Appl. Phys. **117**, 17D914 (2015).

[19] B. Rajeswaran, P. Mandal, Rana Saha, E. Suard, A. Sundaresan, and C. N. R. Rao, Chem. Mater. **24**, 3591 (2012).

[20] N. Das, S. Singh, A. G. Joshi, M. Thirumal, V. R. Reddy, L. C. Gupta, and A. K. Ganguli, Inorg. Chem. **56**, 12712 (2017).

[21] R. Sivasamy, P. Venugopal, and R. Espinoza-González, Mater. Today Commun. **25**, 101603 (2020).

[22] Y. Liu, W. Liu, Y. Li, S. Feng, Z. Zhang, X. Kan, and X. Liu, Ceram. Inter. **49**, 15536 (2023).

[23] J. S. Punitha, A. Nataraj, V. Anbarasu, M. Dhilip, and K. S. Kumar, J. Mater. Sci.: Mater. Electron. **32**, 10266 (2021).

[24] X. Ding, B. Gao, E. Krenkel, C. Dawson, J. C. Eckert, S.-W. Cheong, and V. Zapf, Phys. Rev. B **99**, 014438 (2019).

[25] A. M. Tishin, in *Handbook of Magnetic Materials*, edited by K. H. J. Buschow (North-Holland, Amsterdam, 1999), Vol. 12.

[26] A. M. Tishin and Y. I. Spichkin, in *Condensed Matter Physics*, edited by J. M. D. Coey, D. R. Tilley, and D. R. Vij (IOP, Bristol, 2003).

[27] M. Patra, S. Majumdar, S. Giri, G. N. Iles, and T. Chatterji, J. Appl. Phys. **107**, 076101 (2010).

[28] H. Oesterreicher and F. T. Parker, J. Appl. Phys. **55**, 4334 (1984).

[29] M. D. Kuz'min, M. Richter, and A. M. Tishin, J. Magn. Magn. Mater. **321**, L1 (2009).

[30] L. D. Landau and E. M. Lifshitz, *Electrodynamics of Continuous Media* (Elsevier Butterworth-Heinemann, Oxford, 1999).

[31] J. Lyubina, M. D. Kuz'min, K. Nenkov, O. Gutfleisch, M. Richter, D. L. Schlagel, T. A. Lograsso, and K. A. Gschneidner, Jr., Phys. Rev. B **83**, 012403 (2011).

[32] T. Shang, A. Amon, D. Kasinathan, W. Xie, M. Bobnar, Y. Chen, A. Wang, M. Shi, and M. Medarde, H. Q. Yuan, and T. Shiroka, New J. Phys. **21**, 073034 (2019).

[33] R. Kumar and A. Sundaresan, Phys. Rev. B **106**, 134423 (2022).

[34] S. Chatterjee, P. Dutta, S. Giri, S. Majumdar, S. Sadhukhan, S. Kanungo, S. Chatterjee, M. M. Patidar, G. S. Okram, and V. Ganesan, Phys. Rev. B **102**, 214443 (2020).

[35] A. Banerjee, J. Sannigrahi, S. Giri, and S. Majumdar, Phys. Rev. B **98**, 104414 (2018).

[36] M. Das, P. Sarkar, and P. Mandal, Phys. Rev. B **101**, 144433 (2020).

[37] N. W. Ashcroft and N. D. Mermin, *Solid State Physics* (Cengage Learning, Boston, 1976), Chap. 23, p. 462.

[38] E. Palacios, J. A. Rodríguez-Velamazán, M. Evangelisti, G. J. McIntyre, G. Lorusso, D. Visser, L. J. deJongh, and L. A. Boatner, Phys. Rev. B **90**, 214423 (2014).

[39] V. K. Pecharsky and K. A. Gschneidner, Phys. Rev. Lett. **78**, 4494 (1997).

[40] M. Das, S. Roy, N. Khan, and P. Mandal, Phys. Rev. B **98**, 104420 (2018).

[41] K. Dey, A. Indra, S. Majumdar, and S. Giri, J. Mater. Chem. C **5**, 1646 (2017).

[42] Y. S. Tang, S. M. Wang, L. Lin, Cheng Li, S. H. Zheng, C. F. Li, J. H. Zhang, Z. B. Yan, X. P. Jiang, and J.-M. Liu, Phys. Rev. B **100**, 134112 (2019).

[43] S. Mukherjee, G. Manna, P. Saha, S. Majumdar, and S. Giri, Phys. Rev. Mater. **6**, 054407 (2022).

[44] A. Indra, K. Dey, J. K. Dey, S. Majumdar, U. Rütt, O. Gutowski, M. v. Zimmermann, and S. Giri, Phys. Rev. B **98**, 014408 (2018).

[45] A. Ghosh, K. Dey, M. Chakraborty, S. Majumdar, and S. Giri, Europhys. Lett. **107**, 47012 (2014).

[46] K. Dey, A. Indra, S. Mukherjee, S. Majumdar, J. Strempfer, O. Fabelo, E. Mossou, T. Chatterji, and S. Giri, Phys. Rev. B **100**, 214432 (2019).

[47] J. K. Dey, A. Chatterjee, S. Majumdar, A.-C. Dippel, O. Gutowski, M. v. Zimmermann, and S. Giri, Phys. Rev. B **99**, 144412 (2019).

[48] C. De, S. Ghara, and A. Sundaresan, Solid State Commun. **205**, 61 (2015).

[49] N. Terada, Y. S. Glazkova, and A. A. Belik, Phys. Rev. B **93**, 155127 (2016).

[50] T. N. M. Ngo, U. Adem, and T. T. M. Palstra, Appl. Phys. Lett. **106**, 152904 (2015).

[51] X. Moya, S. Kar-Narayan, and N. D. Mathur, Nat. Mater. **13**, 439 (2014).

[52] K. Dey, A. Indra, A. Karmakar, and S. Giri, J. Magn. Magn. Mater. **498**, 166090 (2020).

[53] C. Dhanasekhar, A. K. Das, and A. Venimadhav, J. Magn. Magn. Mater. **418**, 76 (2016).

[54] J. Krishna Murthy and A. Venimadhav, J. Phys. D: Appl. Phys. **47**, 445002 (2014).

[55] M. P. Singh, K. D. Truong, S. Jandl, and P. Fournier, Phys. Rev. B **79**, 224421 (2009).

[56] C. Meyer, P. Ksoll, V. Roddatis, and V. Moshnyaga, Crystals **11**, 747 (2021).

[57] B. J. Campbell, H. T. Stokes, D. E. Tanner, and D. M. Hatch, J. Appl. Crystallogr. **39**, 607 (2006).

[58] A. Ghosh, A. Pal, K. Dey, S. Majumdar, and S. Giri, J. Mater. Chem. C **3**, 4162 (2015).

[59] A. Indra, K. Dey, A. Midya, P. Mandal, O. Gutowski, U. Rütt, S. Majumdar, and S. Giri, J. Phys.: Condens. Matter **28**, 166005 (2016).

[60] M. E. Zhitomirsky, Phys. Rev. B **67**, 104421 (2003).

[61] S. Pakhira, C. Mazumdar, R. Ranganathan, S. Giri, and M. Avdeev, Phys. Rev. B **94**, 104414 (2016).
[62] Y. Tokiwa, S. Bachus, K. Kavita, A. Jesche, A. A. Tsirlin, and P. Gegenwart, Commun. Mater. **2**, 42 (2021).
[63] J. Krishna Murthy, K. D. Chandrasekhar, S. Mahana, D. Topwal, and A. Venimadhav, J. Phys. D: Appl. Phys. **48**, 355001 (2015).
[64] R. S. Silva, Jr., J. Gainza, C. dos Santos, J. E. F. S. Rodrigues, C. Dejoie, Y. Huttel, N. Biskup, N. M. Nemes, J. L. Martínez, N. S. Ferreira, and J. A. Alonso, Chem. Mater. **35**, 2439 (2023).
[65] Z. Yang, J.-Y. Ge, S. Ruan, H. Cui, and Y.-J. Zeng, J. Mater. Chem. C. **9**, 6754 (2021).
[66] L. Li, P. Xu, S. Ye, Y. Li, G. Liu, D. Huo, and M. Yan, Acta Mater. **194**, 354 (2020).
[67] Y. Zhang, Y. Tian, Z. Zhang, Y. Jia, B. Zhang, M. Jiang, J. Wang, and Z. Ren, Acta Mater. **226**, 117669 (2022).
[68] Z. Dong and S. Yin, Ceram. Int. **46**, 1099 (2020).
[69] B. Wu, Y. Zhang, D. Guo, J. Wang, and Z. Ren, Ceram. Int. **47**, 6290 (2021).
[70] D. V. Karpinsky, I. O. Troyanchuk, and V. V. Sikolenko, J. Phys.: Condens. Matter **19**, 036220 (2007).
[71] D. Yang, T. Yang, P. Mukherjee, S. E. Dutton, D. Huo, and M. A. Carpenter, Phys. Rev. B **99**, 094314 (2019).
[72] J. P. Palakkal, C. R. Sankar, A. P. Paulose, and M. R. Varma, J. Alloys Compd. **743**, 403 (2018).
[73] R. Vilarinho, D. J. Passos, E. C. Queirós, P. B. Tavares, A. Almeida, M. C. Weber, M. Guennou, J. Kreisel, and J. A. Moreira, Phys. Rev. B **97**, 144110 (2018).